





Modeling and improving the output power of terahertz master-oscillator power-amplifier quantum cascade lasers

HAIQING ZHU,^{1,2} HUAN ZHU,¹ CHENREN YU,^{1,2} GAOLEI CHANG,^{1,2} FANGFANG WANG,¹ JIANXIN CHEN,¹ LIANHE LI,³  A. GILES DAVIES,³  EDMUND H. LINFIELD,³  ZHOU TANG,⁴ PINGPING CHEN,⁴ WEI LU,⁴ GANGYI XU,^{1,5,*} AND LI HE¹

¹Key Laboratory of Infrared Imaging Materials and Detectors, Shanghai Institute of Technical Physics, Chinese Academy of Sciences, Shanghai 200083, China

²University of Chinese Academy of Sciences, Beijing 100049, China

³School of Electronic and Electrical Engineering, University of Leeds, Leeds LS2 9JT, UK

⁴National Laboratory of Infrared Physics, Shanghai Institute of Technical Physics, Chinese Academy of Sciences, Shanghai 200083, China

⁵Hangzhou Institute for Advanced Study, University of Chinese Academy of Sciences, Hangzhou 310024, China

*gangyi.xu@mail.sitp.ac.cn

Abstract: A model based on carrier rate equations is proposed to evaluate the gain saturation and predict the dependence of the output power of a terahertz master-oscillator power-amplifier quantum cascade laser (THz-MOPA-QCL) on the material and structure parameters. The model reveals the design rules of the preamplifier and the power extractor to maximize the output power and the wall-plug efficiency. The correction of the model is verified by its agreement with the experiment results. The optimized MOPA devices exhibit single-mode emission at ~ 2.6 THz with a side mode suppression ratio of 23 dB, a pulsed output power of 153 mW, a wall-plug efficiency of 0.22%, and a low divergence angle of $\sim 6^\circ \times 16^\circ$, all measured at an operation temperature of 77 K. The model developed here is helpful for the design of MOPA devices and semiconductor optical amplifiers, in which the active region is based on intersubband transitions.

Published by The Optical Society under the terms of the [Creative Commons Attribution 4.0 License](https://creativecommons.org/licenses/by/4.0/). Further distribution of this work must maintain attribution to the author(s) and the published article's title, journal citation, and DOI.

1. Introduction

Terahertz quantum cascade lasers (THz-QCLs) [1,2] have demonstrated important applications in the fields of spectroscopy, trace gas detection, imaging, and so on [3–9]. Intensive studies have been devoted to improving the performances of single-mode THz-QCLs, including the output power, the wall-plug efficiency and the beam directionality [10–15]. Metal-metal waveguide was widely used in THz-QCLs for high operation temperature due to its high optical confinement factor. However, the mismatch between the mode in the deeply sub-wavelength-thick waveguide and that in the free space degrades severely the output power and the beam directionality. A number of unique photonic concepts have been developed to resolve this issue [16–31]. For examples, THz quantum cascade wire lasers, exploiting a third-order distributed feedback (DFB) grating, exhibited low-divergence beam emission [16]. Developed from that work, the devices utilizing a third-order DFB grating with an asymmetric unit enabled unidirectional emission with improved wall-plug efficiency [17]. Recently, Q. Hu et al. realized a phase-locked array of third-order DFB THz-QCLs via π coupling, showing highly efficient power extraction in continuous wave [18–19]. In addition, cavity configurations such as hybrid Bragg gratings, or

graded photonic heterostructures, were exploited to excite a symmetric mode with high radiation efficiency, which resulted in pulsed output power in hundreds of milliwatt [22–26]. Very recently, quantum cascade metasurface-based vertical-external-cavity surface emitting lasers realized watt-level output power and a large range of frequency tuning [27–31].

Among these novel laser cavities, master-oscillator power-amplifier (MOPA) is a promising configuration to realize high performance in terms of output power, wall-plug efficiency and beam quality. We recently demonstrated the first master-oscillator power-amplifier quantum cascade laser in the terahertz frequency range (THz-MOPA-QCL) [32,33]. In such a MOPA device, the master-oscillator (MO) section is a first-order DFB laser, while the power-amplifier (PA) section consists of a preamplifier and a grating coupler. THz wave generated in the MO section is injected into and amplified in the preamplifier, and is finally coupled into the free space by the grating coupler. As reported in Ref. [33], the THz-MOPA-QCLs exhibited stable single-mode emission with a pulsed output power of 136 mW at an operation temperature of 20 K.

Despite the realization of good performances, the mechanism of power amplification and the design rules of THz-MOPA-QCLs are still need to be clear, and one of the key issues is the gain saturation. In the PA section, when the stimulated emission becomes comparable to the nonradiative recombination, the population inversion and hence the material gain will decrease with the optical power, causing the so called gain saturation. Gain saturation has been extensively studied in semiconductor MOPA devices and semiconductor optical amplifiers (SOA) based on interband transition [34–37]. However, it was seldom studied in the devices based on intersubband transition, such as quantum cascade lasers or amplifiers [38–41]. Considering the significant distinctions between these two transitions, it is necessary to evaluate theoretically and experimentally the gain saturation in the intersubband devices. Especially, in our MOPA devices, both the preamplifier and the grating coupler experience the gain saturation, which makes the analysis more complicated.

In this work, starting from the carrier rate equations of the QCLs [39], we developed a quantitative model to describe the gain saturation in THz-MOPA-QCLs, and calculated the structure dependence of the output power and the wall-plug efficiency. The validity of the model is confirmed by its agreement with the measurements. Guided by the model, we figured out the design rules of the THz-MOPA-QCLs to maximize the output power and the wall-plug efficiency. The optimized MOPA devices demonstrate high performances in terms of side mode suppression ratio (SMSR), output power, and beam directionality.

2. Device structure and modeling

Figure 1(a) shows the scheme of a THz-MOPA-QCL where a metal-metal waveguide is used. The GaAs/Al_{0.15}Ga_{0.85}As active region is based on a design of bound-to-continuum transition, and is the same as that in Ref. [42]. The Al_{0.15}Ga_{0.85}As/GaAs layer sequence in each period of the active region is **5.5**/11.0/**1.8**/11.5/**3.8**/9.4/**4.2**/18.4 (nm), in which GaAs layers are in roman, Al_{0.15}Ga_{0.85}As layers are in bold, and the underlined number corresponds to the doped layer. The laser core contains 180 periods with a total thickness of ~ 11.8 μm, and the measured central emission frequency is ~2.6 THz. The MO section is a first-order DFB laser featuring a buried grating, whose structure parameters were optimized to maximize the seed power [33]. The PA section consists of a straight or tapered preamplifier and a grating coupler. Here, the grating coupler is carefully designed to reduce the residual reflectivity down to the order of 1%, which is important to suppress self-lasing in the PA section. Absorbing boundaries, formed by the uncovered high-loss n⁺ GaAs top contact layer, are set on both ends of the device and also on both lateral sides of the ridge. In consequence, THz wave generated in the MO section is injected into and amplified in the preamplifier, and is finally radiated into the free space via the grating coupler. Figure 1(b) is an SEM picture of such THz-MOPA-QCLs.

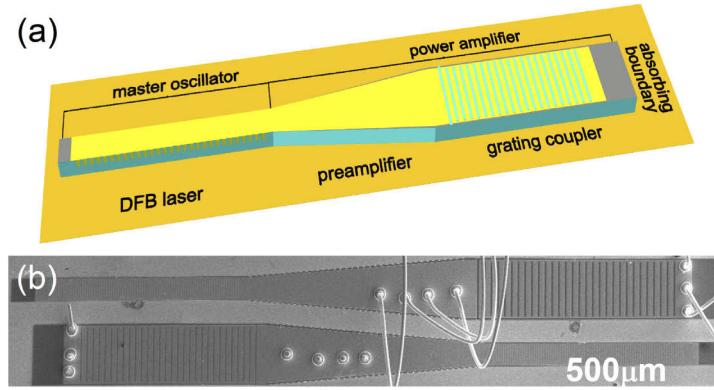


Fig. 1. (a) Schematic illustration of a THz-MOPA-QCL based on a metal-metal waveguide, which consists of a first-order DFB laser, a tapered preamplifier, and a grating coupler. The gray layers correspond to the n^+ GaAs top contact layers which act as the absorbing boundaries. (b) SEM picture of two THz-MOPA-QCLs.

The output power P_{out} of a THz-MOPA-QCL can be expressed as

$$P_{out} = P_{MO} \times \kappa_{amp} \times \eta_{GC}, \quad (1)$$

where P_{MO} is the seed power of the MO section, κ_{amp} the amplification factor of the preamplifier, and η_{GC} the radiation efficiency of the grating coupler. In this work, peak values of the output power (P_{out}) and the wall-plug efficiency (η_{WP}) are considered, which correspond to the operating voltage at resonance. Since both the preamplifier and the grating coupler contain the active region, κ_{amp} and η_{GC} are related to the gain saturation. Therefore, it is necessary to first figure out the dependence of material gain (g) on the optical intensity (I_s).

In a THz-QCL, the rate equation for the electrons in the upper laser level reads [39]

$$\frac{dN_3}{dt} = \frac{J}{ed} - \frac{N_3}{\tau_3} - g_c(N_3 - N_2) \frac{I_s}{h\nu}, \quad (2)$$

where N_3 and N_2 are respectively the 3D electron concentrations of the upper and lower laser levels, g_c the gain cross section, τ_3 the lifetime of the upper laser level, J the driving current density, d the thickness of each period of the active region, and $h\nu$ the photon energy. The material gain g has the form $g = g_c(N_3 - N_2)$. Under the steady-state condition, N_3 writes

$$N_3 = \frac{J\tau_3}{ed} \left(1 + \frac{I_s}{I_{sat}}\right)^{-1} + N_2 \frac{I_s}{I_{sat}} \left(1 + \frac{I_s}{I_{sat}}\right)^{-1}, \quad (3)$$

where I_{sat} is the saturation intensity defined as

$$I_{sat} = \frac{h\nu}{g_c\tau_3} = \frac{h\nu}{\tau_3} \left(\frac{g^*\alpha_{w0}}{\bar{n}_d}\right)^{-1}. \quad (4)$$

Here, the gain cross section g_c is expressed as $g_c = g^*g_{fc} = g^*\alpha_{w0}/\bar{n}_d$, where g^* is the normalized gain cross section, g_{fc} the free carrier absorption cross section, \bar{n}_d the average 3D doping concentration in each period of the active region, α_{w0} the optical loss caused by the free carrier absorption in the active region [39]. Note, the total waveguide loss (α_w) contains not only α_{w0} , but also the loss caused by the n^+ contact layers and the metallic layers. From Eqs. (3) and (4),

the material gain can be expressed as

$$g = g_0 \times \left(1 + \frac{I_s}{I_{sat}} \right)^{-1}, \quad (5)$$

where g_0 is the unsaturated material gain, $g_0 = g_c(J\tau_3/ed - N_2)$. Here, the term $(J\tau_3/ed - N_2)$ refers to the maximum population inversion available in the active region. We note that the expression of gain saturation in intersubband devices, *i.e.* Equation (5), has the similar form as that of interband devices [35]. Equation (4) indicates that, when the optical intensity I_s reaches the saturation intensity I_{sat} , the depopulation rate of N_3 caused by the stimulated radiation is $(N_3 - N_2)/\tau_3 \approx N_3/\tau_3$, which approximately equals to that by the nonradiative recombination. In this case, the material gain decreases to be a half of the unsaturated gain g_0 , as reflected in Eq. (5). On the other hand, since I_{sat} directly relates to the gain cross section and the upper state lifetime, the gain saturation should significantly depend on the operation temperature.

Given the material gain g , the amplification factor κ_{amp} reads

$$\kappa_{amp} = \exp\left[\int_0^{L_{amp}} (g - \alpha_w)dx\right], \quad (6)$$

where x is the propagation distance starting from the import of the preamplifier, and L_{amp} is the length of the preamplifier. As a result, the optical power injected into the grating coupler is $P_{MO} \times \kappa_{amp}$.

To calculate the output power radiated from the grating coupler, we still need to know the optical power as a function of position (x') along the grating coupler, *i.e.*, $P_{GC}(x')$. In the grating coupler, the THz wave experiences not only the amplification caused by the material gain, but also the attenuation caused by the waveguide and radiation losses. Therefore, $P_{GC}(x')$ has the form

$$P_{GC}(x') = P_{MO} \times \kappa_{amp} \times \exp\left[\int_0^{x'} (g - \alpha_w - \alpha_{rad})dv\right]. \quad (7)$$

Here, $x' = 0$ refers to the import of the grating coupler, and α_{rad} is the radiation loss of the grating coupler. The output power of the whole device (P_{out}) can therefore be expressed as

$$P_{out} = \int_0^{L_{GC}} \alpha_{rad} P_{GC}(x') dx'. \quad (8)$$

Here, the integration starts from the import of the grating coupler, and L_{GC} is the length of the grating coupler.

Thus far, we have proposed a model to evaluate the gain saturation and to predict the dependence of the output power on the material and structure parameters for the MOPA device. During the calculation, the material parameters τ_3 and g^* are taken from Ref. [42] since the same active region were used, \bar{n}_d is an experimental value, the structure parameters (α_{w0} , α_w , and α_{rad}) are calculated by the Drude model or the finite element method (FEM) simulations. The only fitting parameters are the seed power P_{MO} , as well as the maximum available population inversion $(J\tau_3/ed - N_2)$. The latter is closely related to the quality of material growth, and determines the unsaturated material gain g_0 . Table 1 lists the values of the related parameters that used in our model.

Table 1. Calculated or experimental values of the parameters used in the model

τ_3 (ps)	\bar{n}_d (cm ⁻³)	α_{w0} (cm ⁻¹)	α_w (cm ⁻¹)	g^*	g_c (cm ²)	I_{sat} (W/cm ²)
12	5.09×10^{15}	11.1	29.6	25.8	5.57×10^{-14}	2.88×10^3

3. Verification of the model

In order to verify the correction of the model, we fabricated and measured a series of THz-MOPA-QCLs. In these devices, the same MO section and grating coupler are used, while straight or tapered preamplifiers are exploited, whose length varies from 100 μm to 1500 μm . The DFB grating contains 80 periods with a central π -shift, and the periodicity (Λ_{DFB}) is 16.2 μm . The grating coupler contains 10 periods with a periodicity (Λ_{GC}) of 46 μm . The radiation loss (α_{rad}) of the grating coupler is 33 cm^{-1} , calculated by 3D FEM with a commercial solver (COMSOL Multiphysics). The ridge widths of the MO section and the grating coupler are respectively 150 μm and 600 μm . The width of the straight preamplifier is the same as that of the MO section. For the tapered preamplifiers, the tapering angle is $\sim 10^\circ$ which is sufficient for beam expansion.

The fabrication of the THz-MOPA-QCLs was similar to that in Ref. [33]. The laser spectra were measured by a Fourier transform infrared spectrometer (Bruker 80V) with a spectral resolution of 0.1 cm^{-1} . The light-current-voltage (L - I - V) curves were measured in pulsed mode with a duty cycle of 1% (the repeated frequency is 10 kHz, and the pulse width is 1 μs), at 20 K. The emission power was measured by a Golay cell which was calibrated by a Thomas Keating absolute terahertz power-meter. The emission spectra of all the devices confirm single mode emission and the side mode suppression ratio (SMSR) is larger than 20 dB. Figures 2(a) and 2(b) show the dependence of the peak output power (P_{out}) and the wall-plug efficiency (η_{WE}) on the length of the straight or tapered preamplifier (L_{amp}). The symbols are the measured results, and the curves show the calculated results. The inset of Fig. 2(a) shows the evolution of the material gain as a function of optical intensity in the waveguide, calculated by Eq. (5). Besides the parameters listed in Table 1, the only fitting data are the seed power P_{MO} and the unsaturated material gain g_0 . As shown in Figs. 2(a) and 2(b), reasonable agreements between the calculated and the measured results are achieved when P_{MO} and g_0 are respectively set as 19 mW and 75 cm^{-1} . The agreements will be further confirmed later, where more devices with different structure parameters were measured.

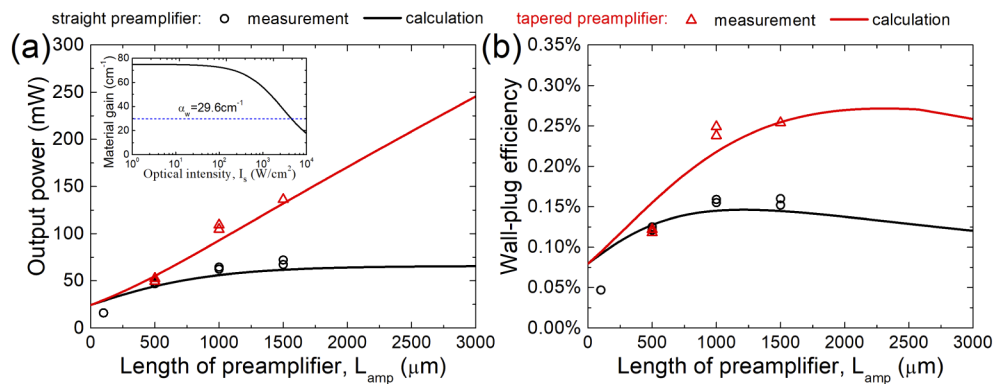


Fig. 2. The output power (a) and wall-plug efficiency (b) of MOPA devices as a function of the length of the preamplifier L_{amp} . The open triangles and circles are the experimental data, and the solid curves show the calculated results. The black symbols and curves correspond to the devices with a straight preamplifier, while the red ones correspond to those with a tapered preamplifier. The inset of the panel (a) is the calculated material gain as a function of optical intensity inside the waveguide. All these devices have the same structures of the MO section and the grating coupler. The DFB grating contains 80 periods, with a periodicity (Λ_{DFB}) of 16.2 μm , and a duty cycle of 75%. The grating coupler contains 10 periods, with a periodicity (Λ_{GC}) of 46 μm , and a slit width of 14 μm .

Figures 2(a) and 2(b) show that, when the straight preamplifier is longer than 1000 μm , P_{out} increases very slowly and η_{WP} starts to decrease, indicating severe gain saturation. For the tapered preamplifier, the lateral expansion of the THz wave weakens the effect of gain saturation. Therefore, when $L_{amp} \geq 1000 \mu\text{m}$, devices with the tapered preamplifier exhibit considerable higher P_{out} and η_{WP} than those with the straight preamplifier. The calculations indicate, even for the tapered preamplifier, when $L_{amp} \geq 2000 \mu\text{m}$, the lateral expansion of the THz wave cannot fully compensate the increase of the optical intensity. This degrades the material gain, and finally decreases the wall-plug efficiency, as shown in Fig. 2(b). On the other hand, due to the reflection caused by the DFB grating and the grating coupler, a long preamplifier may cause self-lasing in the PA section. Consequently, in our MOPA device the optimal L_{amp} is $\sim 1500 \mu\text{m}$, with which the calculated η_{WP} is near the maximum value.

4. Design rules of the grating coupler

For the grating coupler, the behavior of gain saturation relates to the initial optical intensity injected into it, the unsaturated material gain, the waveguide and the radiation loss. It makes the optimization of the grating coupler complicated. Here, we map the dependence of the wall-plug efficiency (η_{WP}) on the radiation loss (α_{rad}) and the length of the grating coupler (L_{GC}), which provides an illuminating insight into the design rules of the grating coupler. Figures 3(a) and 3(b) show the calculation results, where two different lengths L_{amp} of the tapered preamplifier (500 μm and 1500 μm) are considered. Note, the color bars in Figs. 3(a) and 3(b) correspond to different scales of η_{WP} . Despite the different values of L_{amp} , the evolution of the wall-plug efficiency follows a similar trend. The dash lines in Figs. 3(a) and 3(b) show the optimized radiation loss as a function of L_{GC} , which leads to the maximum η_{WP} . For a short grating coupler, a large radiation loss α_{rad} is helpful for a high η_{WP} . When the length of the grating coupler increases, the optimized radiation loss decreases to a fixed value, which is 18 cm^{-1} in our case. Such phenomenon is explained in the followings.

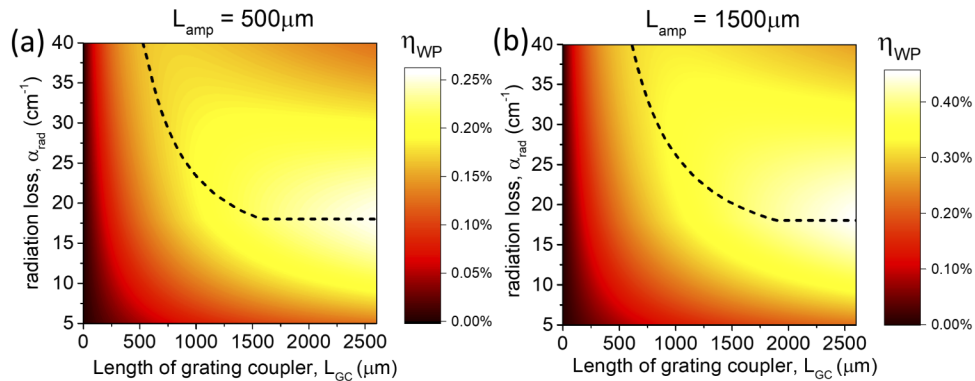


Fig. 3. The calculated wall-plug efficiency as functions of L_{GC} and α_{rad} , where the lengths of the tapered preamplifier are respectively 500 μm (a) and 1500 μm (b). The dash lines show the variation of the optimal radiation loss as a function of L_{GC} , which leads to the maximum wall-plug efficiency.

After propagating for a sufficiently long distance along the grating coupler, the material gain tends to balance the total loss ($\alpha_w + \alpha_{rad}$), and the power of THz wave inside the grating coupler reaches an equilibrium value. From Eq. (5), this equilibrium power reads

$$P_{GC}|_{g=\alpha_{rad}+\alpha_w} = \left(\frac{g_0}{\alpha_{rad} + \alpha_w} - 1 \right) I_{sat} w d_{AR}, \quad (9)$$

where w is the width of the grating coupler, d_{AR} the thickness of the active region. Substituting Eq. (9) into Eq. (8), one can find that in this equilibrium situation, the radiation power per unit distance dP_{out}/dx' is

$$\left. \frac{dP_{out}}{dx'} \right|_{g = \alpha_{rad} + \alpha_w} = \left(\frac{g_0}{\alpha_{rad} + \alpha_w} - 1 \right) I_{sat} \alpha_{rad} w d_{AR}. \quad (10)$$

Obviously, maximizing the efficiency dP_{out}/dx' will result in the highest wall-plug efficiency η_{WP} . With the aforementioned parameters, the efficiency dP_{out}/dx' peaks when the radiation loss α_{rad} is 18 cm^{-1} , which is in good agreement with the results shown in Figs. 3(a) and 3(b).

5. Improvement of the output power and the wall-plug efficiency

The model provides the design rules of the THz-MOPA-QCLs to improve the output power and the wall-plug efficiency. Considering the material used in this work and the power consumption, the optimized values of the tapered preamplifier length L_{amp} , the radiation loss α_{rad} and the number of periods of the grating coupler (N_{GC} , corresponding to the length of the grating coupler) are $1500 \mu\text{m}$, 18 cm^{-1} and 30, respectively. Including the optimized structure, we fabricated four groups of MOPA devices to systematically test the correction of our model. All the devices have the same MO section, where the DFB grating contains 80 periods with a periodicity of $16.2 \mu\text{m}$ and a duty cycle of 75%. Table 2 lists the parameters of the preamplifier and the grating coupler used in these four groups. Two different tapered preamplifier lengths were selected, one is the optimized value ($1500 \mu\text{m}$) and the other is much shorter ($500 \mu\text{m}$). For each preamplifier length, two different radiation losses (18 cm^{-1} and 33 cm^{-1}) were compared, one is close to and the other is significantly larger than the optimized value. In each group, N_{GC} varies from 5 to 30.

Table 2. Parameters of the preamplifier and grating coupler in the fabricated MOPA devices^a

Group	L_{amp} (μm)	α_{rad} (cm^{-1})	N_{GC}
A	500	33 cm^{-1}	5, 10, 15, 20, 25, 30
B	500	18 cm^{-1}	5, 10, 15, 20, 25, 30
C	1500	33 cm^{-1}	10, 20, 30
D	1500	18 cm^{-1}	10, 20, 30

^aFor the grating coupler with a high α_{rad} (33 cm^{-1}), the periodicity and slit width are respectively $46 \mu\text{m}$ and $14 \mu\text{m}$. For that with a low α_{rad} (18 cm^{-1}), the related values are $41 \mu\text{m}$ and $6.5 \mu\text{m}$, respectively.

Up to 36 devices were measured in pulsed mode at 20K, and the results are summarized in Fig. 4. Figure 4(a) shows the emission spectra of some representative devices biased at the level of the maximum output. All devices exhibit single-mode emission and the emission wavelengths are fixed at $\sim 116 \mu\text{m}$, and the side-mode suppression ratio (SMSR) exceeds 25 dB. The linewidth of the laser emission is about 4.5 GHz, which is close to the spectral resolution of the FTIR (3.0 GHz) and is a typical value for a THz-QCL operating in pulsed mode. The emission spectra suggest that the wavelength is determined by the periodicity of the DFB grating and the self-lasing in the PA section is suppressed.

In Figs. 4(b)–4(e), the black squares and red circles present the measured P_{out} and η_{WP} as a function of N_{GC} (number of periods in the grating coupler), with different values of the radiation loss α_{rad} and the preamplifier length L_{amp} . Correspondingly, the black and red curves plot the calculated P_{out} and η_{WP} . We would like to emphasize that all the parameters used in the calculations have been described above, with no additional fitting data. For all devices investigated, the calculated results are in good agreement with the measurements.

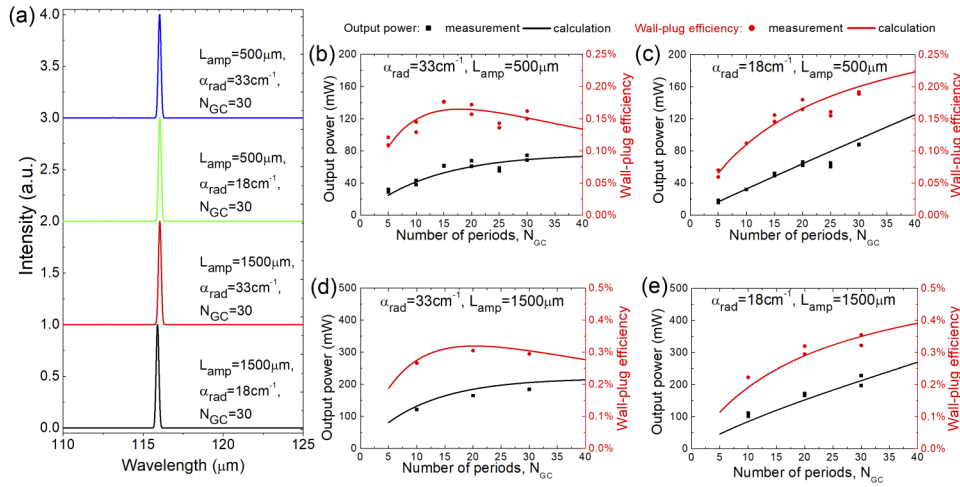


Fig. 4. (a) Emission spectra of some representative THz-MOPA-QCLs, measured at the level of maximum output. For each device, the length of the preamplifier (L_{amp}), the radiation loss (α_{rad}) and the number of periods of the grating coupler (N_{GC}) are marked in the figure. Panels (b) – (e) show the measured and calculated output power and wall-plug efficiency of the 4 groups of the MOPA devices. The values of α_{rad} and L_{amp} for each group are marked in the corresponding panel. The black squares and red circles are the measured output power and wall-plug efficiency, respectively. The black and red lines correspond to the output power and wall-plug efficiency calculated by our model. All devices were measured under the same conditions at 20 K.

Since some calculated parameters are used in the model and contain uncertainty, it is necessary to investigate the robustness of the model, as well as the sensitivity of the fitting parameters (P_{MO} and g_0) to the uncertainty of the calculated parameters. We artificially change α_w (from 20cm^{-1} to 40cm^{-1}) or τ_3 (from 6 ps to 18 ps) – each time only one parameter is changed and the others in Table 1 are unchanged – and we find that the model matches reasonably with the measurements by modifying the two fitting parameters. The modification ranges of P_{MO} and g_0 are respectively from 17 mW to 20 mW and from 59cm^{-1} to 91cm^{-1} , both of which are reasonable. We note that, although the same active region was exploited, the value of g_0 deduced in this work is less than that in Ref. [42], which was computed by density matrix method. One possible reason is the deviation of the doping concentration, since the maximum operation temperature of the Fabry-Perot lasers fabricated from our material is also lower than that in Ref. [42].

Figure 4 clearly shows that, devices with the long preamplifier ($1500\mu\text{m}$) have higher P_{out} and η_{WP} , which are at least twice those with the short preamplifier ($500\mu\text{m}$). We thus focus on the devices with the long preamplifier. Figures 4(d) and 4(e) illustrate that, for devices with the optimized α_{rad} (18cm^{-1}), both P_{out} and η_{WP} increase with the number of periods of the grating coupler N_{GC} . The maximum output power reaches 228 mW when $N_{\text{GC}} = 30$, and the corresponding wall-plug efficiency is 0.36%. However, when α_{rad} (33cm^{-1}) is significantly larger than the optimized value, P_{out} increases slowly, while η_{WP} first rises and then decreases with N_{GC} . Such experimental results are in consistency with the design rules of the grating coupler guided by our model.

Figure 5 presents detailed performances of an optimized MOPA device ($L_{\text{amp}} = 1500\mu\text{m}$, $\alpha_{\text{rad}} = 18\text{cm}^{-1}$, $N_{\text{GC}} = 30$). Figure 5(a) shows the light-current density-voltage (L - J - V) curves of the device at different operation temperatures. The P_{out} and η_{WP} respectively peak at 228mW and 0.36% at 20 K, and remain 153 mW and 0.22% at 77 K. The maximum operation temperature reaches 105 K. Figure 5(b) gives the laser spectrum measured at 77 K, demonstrating single mode

emission with a SMSR of 23 dB. The far-field beam pattern of the device was measured with a Golay cell detector, which was scanned on a 15-cm-radius sphere centered on the device surface. Figure 5(c) shows the angular definition of the far-field measurement. As shown in Fig. 5(d), a single-lobed beam pattern is achieved and the full width at half maximum (FWHM) of the beam divergence is $\sim 6^\circ \times 16^\circ$. Due to the large value of N_{GC} , the effective emission aperture becomes a rectangle which results in an elliptical beam pattern. For another THz-MOPA-QCL with a small value of N_{GC} ($N_{GC} = 10$), whose beam divergence is $\sim 21^\circ \times 36^\circ$, we realized the beam focusing via two off-axis parabolic mirrors. As shown in Fig. 5(e), recorded by a THz camera (Swiss Terahertz, RIGI M1), the waist point of the focused beam is as small as $\sim 250 \mu\text{m} \times 260 \mu\text{m}$.

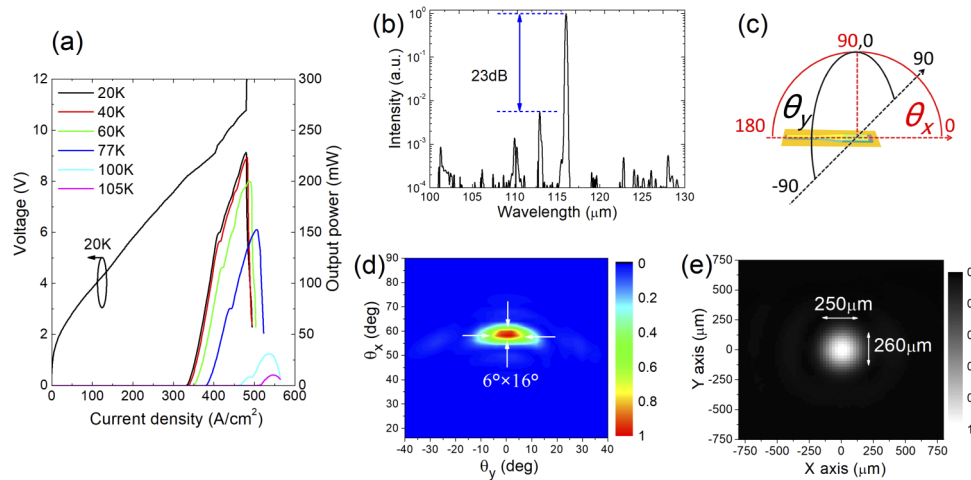


Fig. 5. (a) Light-current density-voltage (L - J - V) curves of an optimized THz-MOPA-QCL, measured at different operation temperature in pulsed mode (10 kHz repeat frequency, 1 μs pulse width). For this device, L_{amp} is 1500 μm , α_{rad} is 18 cm^{-1} and N_{GC} is 30. (b) Emission spectrum of the same device biased at the level of maximum output at 77 K. (c) Schematic angular definition of the far-field measurement. The angle $\theta_x = \theta_y = 0$ responds to the direction along the device ridge. (d) Measured far-field beam pattern of the same device. The divergence angle is $\sim 6^\circ \times 16^\circ$. (e) Focal spot of another MOPA device ($N_{GC} = 10$) measured by a THz camera at 77 K. The emission frequency of the device is $\sim 2.69 \text{ THz}$ and the divergence angle of the emission beam is $\sim 21^\circ \times 36^\circ$.

For performance comparisons, conventional second-order DFB lasers based on the metal-metal waveguide were also fabricated in the same chip. The structure parameters of the second-order DFB lasers were optimized to maximize the output power [24]. The second-order DFB lasers exhibit a peak P_{out} of 2.4 mW and a maximum η_{WP} of 0.025% at 77 K, and the maximum operation temperature is 113 K. The results demonstrate that, at the operation temperature of liquid nitrogen which is interesting for many applications, the output power and the wall-plug efficiency of the MOPA laser are respectively 64 times and 9 times those of the second-order DFB lasers.

Our model suggests that optimizations of the material and device structure will further improve the peak output and the wall-plug efficiency of the THz-MOPA-QCL in pulsed mode. Such optimizations include improving the unsaturated gain of the active region, reducing the gain saturation by exploiting a preamplifier with a larger tapered angle (which means a narrower ridge in the MO section), as well as utilizing a longer grating coupler with a proper radiation loss. However, it is more challenging to realize high output power in continuous wave for the THz-MOPA-QCLs, since the devices developed here have relatively large dimensions which

cause large power consumption. Nevertheless, the MOPA configuration developed in this work indicates that – depend on the design – a gain endowed grating can act as a mode selector, as well as a power extractor with controllable radiation efficiency. A judicious combination of these unique characteristics may lead to novel laser structures featuring low power consumption and high radiation efficiency.

6. Conclusions

We have proposed a model based on the carrier rate equations to evaluate the gain saturation in the THz-MOPA-QCLs. The model furthermore predicts the dependence of the output power and the wall-plug efficiency of a MOPA device on the material and structure parameters. The correction of the model is supported by its agreement with the measured results of a large number of MOPA devices. Guided by the model, single-mode THz-MOPA-QCLs with high pulsed output power, improved wall-plug efficiency and good beam quality have been demonstrated. Our MOPA devices also exhibit possible applications in terahertz near-field microscope due to the small focal spot size.

The model developed in this work is useful to analyze the gain saturation in active regions based on intersubband transition, and can guide the design of the related MOPA and semiconductor optical amplifiers.

Funding

National Natural Science Foundation of China (61574149, 61734006, 61974151); National Key Research and Development Program of China (2016YFA0202200, 2016YFB0402303); Chinese Academy of Sciences (Hundred Talents Program); Engineering and Physical Sciences Research Council (EP/J017671/1); Royal Society; Wolfson Foundation.

Acknowledgment

We thank Dr. Mostafa Shalaby from Swiss Terahertz LLC for lending us a terahertz camera.

Disclosures

The authors declare no conflicts of interest related to this article.

References

1. R. Kohler, A. Tredicucci, F. Beltram, H. E. Beere, E. H. Linfield, A. G. Davies, D. A. Ritchie, R. C. Iotti, and F. Rossi, "Terahertz semiconductor-heterostructure laser," *Nature* **417**(6885), 156–159 (2002).
2. B. Williams, "Terahertz Quantum-cascade Lasers," *Nat. Photonics* **1**(9), 517–525 (2007).
3. Y. Ren, J. N. Hovenier, R. Higgins, J. R. Gao, T. M. Klapwijk, S. C. Shi, A. Bell, B. Klein, B. S. Williams, S. Kumar, Q. Hu, and J. L. Reno, "Terahertz heterodyne spectrometer using a quantum cascade laser," *Appl. Phys. Lett.* **97**(16), 161105 (2010).
4. M. I. Amanti, G. Scalari, M. Beck, and J. Faist, "Stand-alone system for high-resolution, real-time terahertz imaging," *Opt. Express* **20**(3), 2772–2778 (2012).
5. S. Borri, P. Patimisco, A. Sampaolo, H. E. Beere, D. A. Ritchie, M. S. Vitiello, G. Scamarcio, and V. Spagnolo, "Terahertz quartz enhanced photo-acoustic sensor," *Appl. Phys. Lett.* **103**(2), 021105 (2013).
6. L. Consolino, S. Bartalini, H. E. Beere, D. A. Ritchie, M. S. Vitiello, and P. De Natale, "THz QCL-Based Cryogen-Free Spectrometer for in Situ Trace Gas Sensing," *Sensors* **13**(3), 3331–3340 (2013).
7. S. M. Kim, F. Hatami, J. S. Harris, A. W. Kurian, J. Ford, D. King, G. Scalari, M. Giovannini, N. Hoyler, J. Faist, and G. Harris, "Biomedical terahertz imaging with a quantum cascade laser," *Appl. Phys. Lett.* **88**(15), 153903 (2006).
8. P. Dean, N. K. Saat, S. P. Khanna, M. Salih, A. Burnett, J. Cunningham, E. H. Linfield, and A. G. Davies, "Dual-frequency imaging using an electrically tunable terahertz quantum cascade laser," *Opt. Express* **17**(23), 20631–20641 (2009).
9. A. Rahman, A. K. Rahman, and B. Rao, "Early detection of skin cancer via terahertz spectral profiling and 3D imaging," *Biosens. Bioelectron.* **82**, 64–70 (2016).
10. F. Castellano, L. Li, E. H. Linfield, A. G. Davies, H. E. Beere, D. A. Ritchie, and M. S. Vitiello, "THz waveguide adapters for efficient radiation out-coupling from double metal THz QCLs," *Opt. Express* **23**(4), 5190 (2015).

11. Y. Zeng, G. Liang, H. K. Liang, S. Mansha, B. Meng, T. Liu, X. Hu, J. Tao, L. Li, A. G. Davies, E. H. Linfield, Y. Zhang, Y. Chong, and Q. J. Wang, "Designer Multimode Localized Random Lasing in Amorphous Lattices at Terahertz Frequencies," *ACS Photonics* **3**(12), 2453–2460 (2016).
12. S. Schönhuber, M. Brandstetter, T. Hirsch, C. Deutsch, M. Krall, H. Detz, A. M. Andrews, G. Strasser, S. Rotter, and K. Unterrainer, "Random lasers for broadband directional emission," *Optica* **3**(10), 1035–1038 (2016).
13. F. Wang, I. Kundu, L. Chen, L. Li, E. H. Linfield, A. G. Davies, S. Moudji, R. Colombelli, J. Mangeney, J. Tignon, and S. S. Dhillon, "Engineered far-fields of metal-metal terahertz quantum cascade lasers with integrated planar horn structures," *Opt. Express* **24**(3), 2174–2182 (2016).
14. C. Yu, H. Zhu, F. Wang, G. Chang, H. Zhu, J. Chen, P. Chen, Z. Tang, W. Lu, C. Shen, T. Jiang, X. Wang, W. Wu, G. Xu, and L. He, "Highly efficient power extraction in terahertz quantum cascade laser via a grating coupler," *Appl. Phys. Lett.* **113**(12), 121114 (2018).
15. F. Y. Zhao, Y. Y. Li, J. Q. Liu, F. Q. Liu, J. C. Zhang, S. Q. Zhai, N. Zhuo, L. J. Wang, S. M. Liu, and Z. G. Wang, "Sampled grating terahertz quantum cascade lasers," *Appl. Phys. Lett.* **114**(14), 141105 (2019).
16. M. I. Amanti, M. Fischer, G. Scalari, M. Beck, and J. Faist, "Low-divergence single-mode terahertz quantum cascade laser," *Nat. Photonics* **3**(10), 586–590 (2009).
17. A. Khalatpour, J. L. Reno, N. P. Kherani, and Q. Hu, "Unidirectional photonic wire laser," *Nat. Photonics* **11**(9), 555–559 (2017).
18. S. Biasco, K. Garrasi, F. Castellano, L. Li, H. E. Beere, D. A. Ritchie, E. H. Linfield, A. G. Davies, and M. S. Vitiello, "Continuous-wave highly-efficient low-divergence terahertz wire lasers," *Nat. Commun.* **9**(1), 1122–1128 (2018).
19. A. Khalatpour, J. L. Reno, and Q. Hu, "Phase-locked photonic wire lasers by π coupling," *Nat. Photonics* **13**(1), 47–53 (2019).
20. Y. Halioua, G. Xu, S. Moudji, L. Li, J. Zhu, E. H. Linfield, A. G. Davies, H. E. Beere, D. A. Ritchie, and R. Colombelli, "Phase-locked arrays of surface-emitting graded-photonic-heterostructure terahertz semiconductor lasers," *Opt. Express* **23**(5), 6915–6923 (2015).
21. T. Kao, J. L. Reno, and Q. Hu, "Phase-locked laser arrays through global antenna mutual coupling," *Nat. Photonics* **10**(8), 541–546 (2016).
22. L. Mahler, A. Tredicucci, F. Beltram, C. Walther, J. Faist, H. E. Beere, and D. A. Ritchie, "High-power surface emission from terahertz distributed feedback lasers with a dual-slit unit cell," *Appl. Phys. Lett.* **96**(19), 191109 (2010).
23. Y. Jin, L. Gao, J. Chen, C. Wu, J. L. Reno, and S. Kumar, "High power surface emitting terahertz laser with hybrid second- and fourth-order Bragg gratings," *Nat. Commun.* **9**(1), 1407 (2018).
24. G. Xu, R. Colombelli, S. P. Khanna, A. Belarouci, X. Letartre, L. Li, E. H. Linfield, A. G. Davies, H. E. Beere, and D. A. Ritchie, "Efficient power extraction in surface-emitting semiconductor lasers using graded photonic heterostructures," *Nat. Commun.* **3**(1), 952 (2012).
25. G. Xu, Y. Halioua, S. Moudji, R. Colombelli, H. E. Beere, and D. A. Ritchie, "Stable single-mode operation of surface-emitting terahertz lasers with graded photonic heterostructure resonators," *Appl. Phys. Lett.* **102**(23), 231105 (2013).
26. G. Xu, L. Li, N. Isac, Y. Halioua, A. Giles Davies, E. H. Linfield, and R. Colombelli, "Surface-emitting terahertz quantum cascade lasers with continuous-wave power in the tens of milliwatt range," *Appl. Phys. Lett.* **104**(9), 091112 (2014).
27. L. Xu, C. A. Curwen, P. W. C. Hon, Q. Chen, T. Itoh, and B. S. Williams, "Metasurface external cavity laser," *Appl. Phys. Lett.* **107**(22), 221105 (2015).
28. L. Xu, C. A. Curwen, J. L. Reno, and B. S. Williams, "High performance terahertz metasurface quantum-cascade VECSEL with an intra-cryostat cavity," *Appl. Phys. Lett.* **111**(10), 101101 (2017).
29. L. Xu, C. A. Curwen, D. Chen, J. L. Reno, T. Itoh, and B. S. Williams, "Terahertz Metasurface Quantum-Cascade VECSELs: Theory and Performance," *IEEE J. Sel. Top. Quantum Electron.* **23**(6), 1–12 (2017).
30. C. A. Curwen, J. L. Reno, and B. S. Williams, "Terahertz quantum cascade VECSEL with watt-level output power," *Appl. Phys. Lett.* **113**(1), 011104 (2018).
31. C. Curwen, J. Reno, and B. Williams, "Broadband continuous single-mode tuning of a short-cavity quantum-cascade VECSEL," *Nat. Photonics* **13**(12), 855–859 (2019).
32. H. Zhu, F. Wang, Q. Yan, C. Yu, J. Chen, G. Xu, L. He, L. Li, L. Chen, A. Giles Davies, E. H. Linfield, J. Hao, P. Vigneron, and R. Colombelli, "Terahertz master-oscillator power-amplifier quantum cascade lasers," *Appl. Phys. Lett.* **109**(23), 231105 (2016).
33. H. Zhu, H. Zhu, F. Wang, G. Chang, C. Yu, Q. Yan, J. Chen, L. Li, A. G. Davies, E. H. Linfield, Z. Tang, P. Chen, W. Lu, G. Xu, and L. He, "Terahertz master-oscillator power-amplifier quantum cascade laser with a grating coupler of extremely low reflectivity," *Opt. Express* **26**(2), 1942–1953 (2018).
34. B. Hakki and T. Paoli, "Gain spectra in GaAs double-heterostructure injection lasers," *J. Appl. Phys.* **46**(3), 1299–1306 (1975).
35. W. W. Chow and S. W. Koch, *Semiconductor-laser fundamentals: physics of gain materials*. (Springer, 1999).
36. J. Huang and L. W. Casperson, "Gain and saturation in semiconductor lasers," *Opt. Quantum Electron.* **25**(6), 369–390 (1993).
37. P. Parvin, M. Ilchi-Ghazaani, A. Bananej, and Z. Lali-Dastjerdi, "Small signal gain and saturation intensity of a Yb:Silica fiber MOPA system," *Opt. Laser Technol.* **41**(7), 885–891 (2009).

38. V. Gkortsas, C. Wang, L. Kuznetsova, L. Diehl, A. Gordon, C. Jirauschek, M. Belkin, A. Belyanin, F. Capasso, and F. Kärtner, "Dynamics of actively mode-locked Quantum Cascade Lasers," *Opt. Express* **18**(13), 13616–13630 (2010).
39. J. Faist, *Quantum Cascade Lasers*. (Oxford University, 2013).
40. P. Rauter, S. Menzel, A. K. Goyal, B. Gökden, C. A. Wang, A. Sanchez, G. W. Turner, and F. Capasso, "Master-oscillator power-amplifier quantum cascade laser array," *Appl. Phys. Lett.* **101**(26), 261117 (2012).
41. P. Rauter, S. Menzel, A. K. Goyal, C. A. Wang, A. Sanchez, G. Turner, and F. Capasso, "High-power arrays of quantum cascade laser master-oscillator power-amplifiers," *Opt. Express* **21**(4), 4518–4530 (2013).
42. M. I. Amanti, G. Scalari, R. Terazzi, M. Fischer, M. Beck, J. Faist, A. Rudra, P. Gallo, and E. Kapon, "Bound-to-continuum terahertz quantum cascade laser with a single-quantum-well phonon extraction/injection stage," *New J. Phys.* **11**(12), 125022 (2009).